

# Nonvolatile electric control of exciton complex in monolayer MoSe<sub>2</sub> with two-dimensional ferroelectric CuInP<sub>2</sub>S<sub>6</sub>

Xiaoyu Mao<sup>1,2, #</sup>, Jun Fu<sup>1,2, #</sup>, Chen Chen<sup>1,2, #</sup>, Yue Li<sup>1,2</sup>, Heng Liu<sup>1,2</sup>, Ming Gong<sup>3,4, \*</sup>  
and Hualing Zeng<sup>1,2, \*</sup>

1. International Center for Quantum Design of Functional Materials (ICQD), Hefei National Laboratory for Physical Science at the Microscale, and Synergetic Innovation Center of Quantum Information and Quantum Physics, University of Science and Technology of China, Hefei, Anhui 230026, China

2. Key Laboratory of Strongly-Coupled Quantum Matter Physics, Chinese Academy of Sciences, Department of Physics, University of Science and Technology of China, Hefei, Anhui 230026, China

3. CAS Key Laboratory of Quantum Information, University of Science and Technology of China, Hefei, 230026, People's Republic of China

4. Synergetic Innovation Center of Quantum Information and Quantum Physics, University of Science and Technology of China, Hefei, Anhui 230026, China

# Contribute equally to this work

\* Corresponding author

**Abstract:** Monolayer transition metal dichalcogenides (TMDs) have provided a platform to investigate the excitonic states at the two-dimensional (2D) limit. The inherent properties of excitons in TMDs such as the quantum yield, the charge states and even the binding energy, can be effectively controlled via the electrostatic gating, the selective carrier doping or the substrate dielectric engineering. Here, aiming for the nonvolatile electrical tunability of excitonic states and thereby the optical property of TMDs, we demonstrate a 2D ferroelectric heterostructure with monolayer MoSe<sub>2</sub> and ultrathin CuInP<sub>2</sub>S<sub>6</sub> (CIPS). In the heterostructure, the electric polarization of CIPS results in continuous, global, and giant electronic modulation in monolayer MoSe<sub>2</sub>. With the saturated ferroelectric polarization of CIPS, electron-doped or hole-doped MoSe<sub>2</sub> is realized in a single device with a large carrier density tunability up to  $5 \times 10^{12}$

cm<sup>-2</sup>. The nonvolatile behavior of these devices up to three months is also characterized. Our results provide a new and practical strategy for low-power consumption and agelong tunable optoelectronic devices.

## Introduction

The monolayer transition metal dichalcogenides (TMDs) have attract extensive investigations for on the band structure engineering,<sup>1, 2, 3</sup> strong interactions between the electron and holes,<sup>4, 5, 6, 7</sup> and the valley degree of freedom.<sup>8, 9, 10</sup> Among the progresses achieved, tuning the electronic structure is one of the most concerned issues due to their nature as a new class of two-dimensional (2D) direct band gap semiconductor.<sup>11, 12, 13, 14</sup> In general, it can be realized either through chemical doping or applying electrostatic field effect with conventional dielectrics. For example, selectively introducing defects or dopants in monolayer TMDs leads to the formation of p-n junction.<sup>15, 16, 17</sup> Incorporating the field-effect transistor (FET) device, n-type or p-type monolayer TMDs is realized via the electrical gating.<sup>18, 19, 20</sup> However, the chemical way inevitably brings the disorder effect which enhances the carrier scattering and thereby leads to the decreased conductivity and the spectral broadening in TMDs, while the FET structure requests applying the gate voltage to maintain the doping which fails to meet the standard of a low-power consumption device. A disorder-free and nonvolatile scheme is anticipated to overcome the challenges.

Very recently, some new ways based on bulk perovskite ferroelectrics, including the lead zirconate titanate (PZT), P (VDF-TrFE), and lithium niobite, have been utilized to modulate the light emission in 2D TMDs.<sup>21, 22, 23, 24</sup> In these systems, the emission of TMDs can be controlled by the predefined ferroelectric domains with opposite polarizations, which were achieved through strain engineering and tip-enhanced local electric field. However, as the key step for device applications, the continuously and globally ferroelectric tuning of emission in TMDs has yet been reported. One underlying origin is the high poling voltage required in conventional ferroelectrics because of their nature as large bandgap insulators with relatively large film thickness.<sup>25</sup>

Moreover, for oxide perovskite ferroelectrics, the perfect Coulomb screening of electric polarization at the interface relies on rigorous lattice matching, which is difficult to realize when coupling with monolayer TMDs.<sup>26, 27</sup> As a result, the ferroelectric modulation ability is limited in this type of quasi-2D heterostructure.

Here, to resolve the above two major problems, we demonstrate the nonvolatile electric doping effect by constructing a device based on a monolayer MoSe<sub>2</sub> and a 2D ferroelectric CuInP<sub>2</sub>S<sub>6</sub> (CIPS). In this device, a retentive electrostatic field is introduced from the ferroelectric layer without direct coupling between the sample and the dielectric substrate. The device is fabricated via the mechanical stacking method, showing that the spontaneous polarization of the CIPS can provide strong positive and negative electric field, which can induce controllable excitonic states between n-typed and p-typed emission from the photoluminescence (PL) spectra. Good quality in the emission spectra is also demonstrated after three months. We have also studied the physics of exciton and trion peaks at low temperature to the high doping level, in which the long-tail from the three-body recoil effect is observed. The doping capability of the device is estimated to be as high as over  $5 \times 10^{12} \text{ cm}^{-2}$ . Our results provide a new strategy for developing practical 2D ferroelectric heterostructure based optoelectronics.

## Results and discussions

The 2D ferroelectric device is depicted in Figure 1a, in which the CIPS ultrathin flake is sandwiched by the top monolayer MoSe<sub>2</sub> and the bottom Au electrode. In CIPS, the sulfur atoms are covalently interconnected to form a frame and the Cu, In, and P-P pair atoms fill in the sulfur cages with a triangular pattern, respectively. The out-of-plan (OOP) ferroelectricity of CIPS originates from the Cu ion skewing off the inversion symmetry center in each single layer. The polarization in CIPS can be controlled by the bias across the sample. When the bias is applied, the upper and lower surfaces may accumulate opposite charges, which can then influence the carrier doping in the monolayer MoSe<sub>2</sub>. This equivalently induce carrier doping to the monolayer MoSe<sub>2</sub> from the screening effect.

Firstly, we confirm the ferroelectricity of CIPS by performing the piezoresponse

force microscopy (PFM) test on CIPS thin flakes ( $\sim 30$  nm) at ambient condition (see Figure 1b). The phase contrast of  $180^\circ$  between the adjacent domains indicates of antiparallel alignment of the OOP electric polarizations. Moreover, by comparing the Atomic Force Microscope (AFM) measurement and the PFM amplitude image of the same area (see Figure S1), no obvious correlation between the ferroelectric domain structures and the morphology is observed, indicating of clear ferroelectric CIPS.<sup>28</sup>

Next, we show the mechanism of 2D ferroelectric doping in our device. In Figure 1a the top MoSe<sub>2</sub> and the bottom Au electrode not only function as an electric polarization switch, but also serve as the Coulomb screening layers. The induced screening charges by the electric polarization in CIPS result in the shift of the Fermi energy level in MoSe<sub>2</sub>. Consequently, the excitonic optical transitions at K/K' valleys in monolayer MoSe<sub>2</sub> are strongly affected. With this mechanism (see Figure 1c), n-type or p-type doping in MoSe<sub>2</sub> can be realized by controlling the direction of the electric polarization in CIPS to be upward or downward, respectively. Furthermore, from the ferroelectric hysteresis of CIPS (see Figure S1), this type of electronic doping is nonvolatile.

We have prepared and studied 25 ferroelectric devices in total, all of which show similar behaviors. The device fabrication process is detailed in Methods. Figure 2 presents the results from a typical device (termed as Device 1#). This sample has thickness of about 5 nm evidenced from the optical image (Figure 2a) and AFM topography (Figure 2b). This thickness is slightly greater than the switchable polarization in CIPS reported in Ref. 28 with thickness of 4 nm, thus the reversible ferroelectric doping in our device is feasible. We measured the photoluminescence (PL) spectrum from MoSe<sub>2</sub> under 7 K. This spectrum depends strongly on the electric polarization in CIPS, although during the PL measurement the voltage is removed. In Figure 2c and Figure 2d, we present the PL spectrum by scanning the voltage from -5 V to +3 V, and backward, respectively, which yields different behaviors due to the electric hysteresis effect of CIPS. However, the peak position in these conditions are the same as the bare monolayer MoSe<sub>2</sub> (see Figure 2e, with exciton  $X^0$  peak at 1.66 eV and trion  $X^\pm$  at 1.63 eV). No obvious broadening of the spectrum is observed for the three cases in Figure 2e, thus the CIPS only plays the role of carrier doping. In

Figure 2f, we report the electric hysteresis effect from the intensity ratio ( $X^0/X^-$ ) of the PL spectra, which shows a perfect hysteresis curve (see Figure 2f). Since this is a room temperature ferroelectric (with critical temperature  $T_c \sim 320$  K), the similar curve can be observed even under ambient condition (see Figure S2). In Figure S3, we perform the same experiments by replacing CIPS with  $\text{SiO}_2$ , which is a non-ferroelectric material, the similar hysteresis curve is not shown up, showing that the emission is indeed controlled by the electric hysteresis effect of CIPS.

Figure 2f is not the most transparent manifestation of the nonvolatile effect. To this end, in Figure 3, we study the relation between electric polarization and PL spectrum using the PFM tip in Device 3# (see the structure in Figure 3a and Methods), which can induce the flip of polarization by a local electric field in a square region ( $2 \mu\text{m} \times 2 \mu\text{m}$ ). Figure 3b displays the phase image of the artificially created ferroelectric domain structure at room temperature, in which the contrast of  $180^\circ$  indicates the antiparallel polarization directions of the two adjacent domains. After that, we immediately measure the PL mapping in the same region, which is given in Figure 3c, showing that the two regions with antiparallel polarizations exhibit totally different spectrum. At room temperature, a broad peak is observed (see Figure 3d); however, at low temperature, the two peaks ( $X^0$  and  $X^-$ ) can be clearly distinguished in these two regimes (see Figure 3e). This electric polarization can persist for an extraordinarily time. In Figure 3f, we present the same experiments in the same sample after three months, which yield almost the same PL spectrum. This result demonstrates the nonvolatile electric controllability of the exciton state in the monolayer  $\text{MoSe}_2$  by the two-dimensional CIPS.

In addition to the featured nonvolatility, we demonstrate the remarkable gating efficiency of our heterostructure device. With the same ferroelectric device structure, the electrical polarizing method is changed from the pulse mode to the continuous-voltage mode (or DC voltage mode). Figure 4a shows the PL mapping from Device 4# by changing the DC voltage from -4 V to 3 V at 7 K. Differed from the results from Device 1#, except for the  $X^0$  PL peak, the photon emissions from  $X^+$  and  $X^-$  states can be distinguished. For hole and electron trions in monolayer  $\text{MoSe}_2$ , due to the same

binding energy and similar effective mass, there is no observable spectroscopic differences such as peak position or line shape in the PL spectrum. Here, the assignment of the PL peaks to  $X^+$  and  $X^-$  are done through the doping process of the ferroelectric device as discussed and verified previously. In the PL mapping, clear  $X^0$  emissions are observed within the DC voltage ranging from -2 V to -1 V. Therefore, under below -2 V or above -1 V electric poling in the device, different type of doping from the CIPS thin layer leads to the formation of  $X^+$  or  $X^-$  respectively. The observation of hole trions in monolayer MoSe<sub>2</sub> under negative poling voltage indicates the change of its electronic structure from n-type to p-type, which suggests the ultra-high electrostatic doping efficiency of our device if compared with conventional oxide dielectrics-based gating method. The giant gating ability is attributed to the saturated electric polarizations of CIPS under continuous voltage polarizing.

This setup enables us to observe the asymmetry of the  $X^+/X^-$  spectra away from Lorentz lineshape, probably from the absence of disorder during charge doping. As shown in Figure 4b and 4c, under -4 V and +3 V poling, both the  $X^+$  and  $X^-$  PL peaks are asymmetric with long tails at the low energy side. The observed broad lineshape are due to the charge recoil effect stemming from three particles nature of trions. Unlike the radiative recombination of neutral excitons, which occurs only at the Brillouin zone center, excited trions can radiatively decay with non-zero momentum by kicking out an electron or hole. The schematic for the charge recoil effect is shown in Supporting Information Figure S4. With the energy and momentum conservation, the emitted photon energy from the recombination of trions is given by  $\hbar\omega_T = E_{trion}^0 - \frac{M_X}{M_e} E_{KE}$ , where  $E_{trion}^0$  is the zero-momentum trions energy,  $M_X$  is the exciton mass,  $M_e$  is the effective electron (hole) mass,  $E_{KE}$  is the electron (hole) kinetic energy. We fitted the low-energy PL tail with exponential function and extracted the tail length as a function of the DC poling voltage in Figure 4d.<sup>29</sup> The dependence of the tail length with the DC bias originates from the shift of  $E_F$  and the thermal excitation of charge carriers. For the latter contribution, it follows the Boltzmann distribution. Therefore, by fixing the  $E_F$  with DC +3 V, we found that the tail length of  $X^-$  PL peak increased from

10 meV to 30 meV as the temperature changed from 7 K to 180 K (Figure 4e). We also performed excitation power dependence study at DC +3 V poling in Figure 4f. The tail length is almost the same as the laser power varies from 1  $\mu$ W to 100  $\mu$ W. This characteristic behavior, which is independent of laser power but relies on temperature, helps us to exclude the origin of the observed long low-energy tail from the PL of defects and the many-body collision.

Then it is naturally to ask how many electrons and holes can be doped in this way to the monolayer MoSe<sub>2</sub>? The doped carriers are realized from the screening effect, which is the same as the carrier density at the surface of CIPS. For this reason, we replace the MoSe<sub>2</sub> with the single layer graphene. Since the volume of the graphene is much smaller than the CIPS, we expect the influence of graphene on CIPS is small. This platform has the advantage that the Fermi energy is directly given by  $E_F = -sgn(n)\hbar v_F \sqrt{(\pi|n|)}$ , where  $v_F$  ( $\sim 10^6$  m/s) is the Fermi velocity, and  $n$  is the surface charge density. Therefore, the probe on the  $E_F$  of graphene allows the estimation on the charge density  $n$ , which is in mount equal to the induced carrier doping density in the ferroelectric device. The  $E_F$  of graphene can be measured through the Raman spectrum as the change in doping level results in stiffening or softening of the G band phonons.<sup>30, 31, 32</sup> As shown in Figure 5a, the G mode peak shifts with varied poling voltages at 7 K. We summarized the G mode frequency  $\omega_g$  as a function of the poling voltage (Figure 5b), from which we conclude that  $n = 0$  under +2 V voltage modulation. According to previous study, the carrier density  $n$  of graphene follows  $\omega_g$  with

$$\omega_g = \omega_g^0 + \lambda \hbar v_F \sqrt{\pi|n|},$$

where  $\lambda = 0.047$  from our best fitting. The correspondence between charge density  $n$  and poling voltage was converted in Figure 5c. We found that the ferroelectric CIPS layer can induce carrier doping density as high as  $5 \times 10^{12} \text{ cm}^{-2}$  in the heterostructure device, from which we estimate the change of Fermi energy  $E_F$  at about 0.38 eV. This carrier density doping is comparable with that using the conventional doping based on contact dielectric substrate.<sup>33</sup> However, it is necessary to pointing out that the new method can in principle induce much higher carrier density at  $\sim 10^{13} \text{ cm}^{-2}$  with improved

sample quality.<sup>34</sup> Moreover, the doping capability of this heterostructure may be further enhanced by replacing CIPS with some other 2D ferroelectric materials, such as  $\alpha$ - $\text{In}_2\text{Se}_3$ .<sup>35</sup> For this reason, this system may provide a possible way to realize physics in the strong density limit, in which the many-body effect is dominated.

## Conclusion

In summary, we have presented a 2D ferroelectric heterostructure device that is capable to continuously tune the optical property of monolayer  $\text{MoSe}_2$  with electrical nonvolatility. Such retentive electrostatic gating effect originates from the out-of-plane electric polarization in 2D ferroelectric CIPS. To our knowledge, clear charge carrier recoil effect for both electron and hole trions is observed in a single device for the first time. Our results provide a route to develop novel functional nanoelectronic devices with vdW material as well as a method to explore emergent physical properties with 2D ferroelectrics.

## Methods

***Sample preparations and device fabrications.*** Bulk single crystal CIPS in this study was purchased from HQ Graphene, Inc. Bulk single crystal  $\text{MoSe}_2$  was synthesized by chemical vapor transportation method. The ultrathin CIPS and monolayer  $\text{MoSe}_2$  were obtained by mechanical exfoliation on PDMS (Gel-Pak, WF-60-X4). Few-layer CIPS and monolayer  $\text{MoSe}_2$  were prepared on polydimethylsiloxane (PDMS) by mechanical exfoliation method. Using the all-dry transfer method,<sup>36</sup> few-layers CIPS was transferred onto the surface of pre-prepared Au electrode. Monolayer  $\text{MoSe}_2$  was stacked on CIPS thin layer in the same way. By post-stacking  $\text{MoSe}_2$ , two electrodes were bridged, allowing the DC or pulsed voltage applying in the heterostructure devices. The device electrodes were fabricated via standard photoetching method with the deposition of 5 nm titanium and 25 nm gold via e-beam evaporator.

***Electrical polarization process.*** The polarizing pulse voltage was applied through a



Source/Measure unit (Keysight Technologies B2912). The pulse duration period is 0.2s with the width at 0.001 s. Each voltage pulse is repeated for 30 periods. The DC mode tests on Device 4# and Device 4# were performed with the same instrument.

***PFM Measurement:*** PFM measurements were performed with AIST-SmartSPM by using Pt-Ir coated conducting Si tip under ambient condition. The conductive substrates used in this study were prepared through sputtering 30 nm thick gold film onto Si substrate with 90 nm SiO<sub>2</sub> on top. The PFM configuration for ferroelectric domain writing is depicted in Figure 3a. By sweeping the sample surface with applying -5.6 V tip bias, we flipped the polarization direction to be upward in the center with a square region (2  $\mu\text{m}$   $\times$  2  $\mu\text{m}$ ).

***Optical measurements.*** The PL measurement was performed via Princeton Instruments spectrometer (IsoPlane® SCT 320) with continue wave solid-state 532 nm laser. With a home-made microscope set-up, the laser was focused to a spot with the diameter at  $\sim 2$   $\mu\text{m}$ . The laser intensity was kept at below 10  $\mu\text{W}$  to prevent light doping or exciton generation from high-power excitation in all the measurements. When taking the PL spectrum, all the devices were placed in a cryogenic chamber (Montana Instruments), which is capable of tuning sample temperature from 7 K to 300 K.

## **Acknowledgments**

This work was supported by the National Key Research and Development Program of China (Grant No. 2017YFA0205004 and 2018YFA0306600), the National Natural Science Foundation of China (Grant No. 11674295), the Fundamental Research Funds for the Central Universities (Grant No. WK2340000082 and WK2060190084), Anhui Initiative in Quantum Information Technologies (Grant No. AHY170000), and the China Government Youth 1000-Plan Talent Program. This work was partially carried out at the USTC Center for Micro and Nanoscale Research and Fabrication.

## **Author Contributions**

H. Z. conceived the idea and supervised the research. X. M., Y. L., and J. F. prepared the samples. X. M., J. F. and C. C. fabricated the devices, carried out the transport, PFM, and Raman spectrum measurements of the 2D ferroelectric device. X. M., J. F., M. G. and H. Z. analyzed the data, wrote the paper, and all authors commented on the manuscript.

## **Author Information**

The authors declare no competing financial interests. Correspondence and requests for materials should be addressed to Ming Gong ([gongm@ustc.edu.cn](mailto:gongm@ustc.edu.cn)) and Hualing Zeng ([hlzeng@ustc.edu.cn](mailto:hlzeng@ustc.edu.cn)).

## Figures and captions

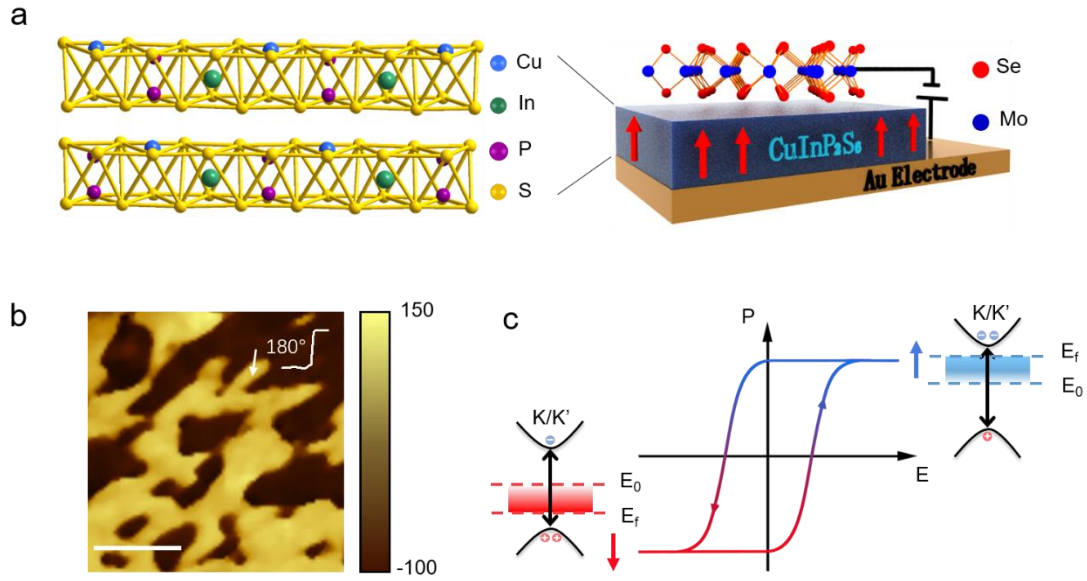


**Figure 1.** Device concept of 2D ferroelectric doping. a) The 3D schematic diagram of the ferroelectric heterostructure. The red arrows indicate the ferroelectric polarization. The zoomed area shows the crystal structure of ferroelectric CIPS. b) The PFM phase of CIPS flakes in the OOP direction, the inset shows the PFM phase along the white arrow. The scale bar is 1  $\mu\text{m}$ . c) The ferroelectric hysteresis loop and the band energy of MoSe<sub>2</sub> at corresponding polarization state. The blue and red arrows indicate the polarization direction of CIPS. The up (down) polarization state of CIPS provides negative (positive) screening charges for MoSe<sub>2</sub>, which induces the n (p) type doping. The Fermi energy shift is shown in the diagram.

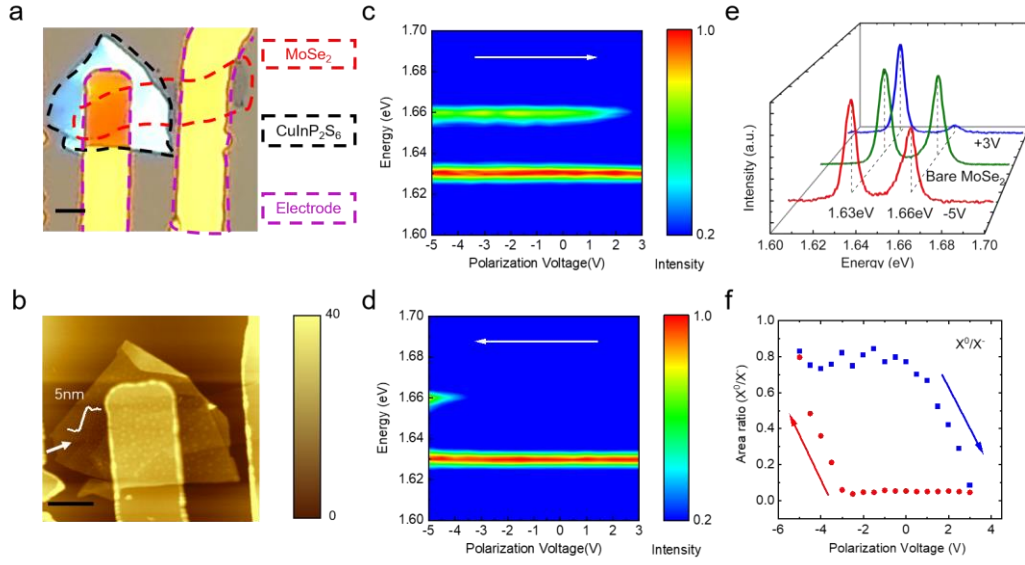


**Figure 2.** Nonvolatile electric modulation on excitonic states. a) The optical image and b) the AFM topography of Device 1#. The monolayer MoSe<sub>2</sub>, few-layers CIPS and electrodes are indicated by red, black, and purple dashed frames, respectively. The thinnest area of CIPS in the device is 5 nm. The scale bar is 3 μm. c) The PL spectrums of MoSe<sub>2</sub> as pulses polarization voltage changes from -5 V to +3 V and d) backward at 7 K. e) The PL spectrum of bare monolayer MoSe<sub>2</sub> (green line) and device 1# after -5 V (red line) and +3 V (blue line) pulses polarization at 7 K. f) The PL intensity ratio of ( $X^0/X^-$ ) depends on pulses polarization voltage variation.

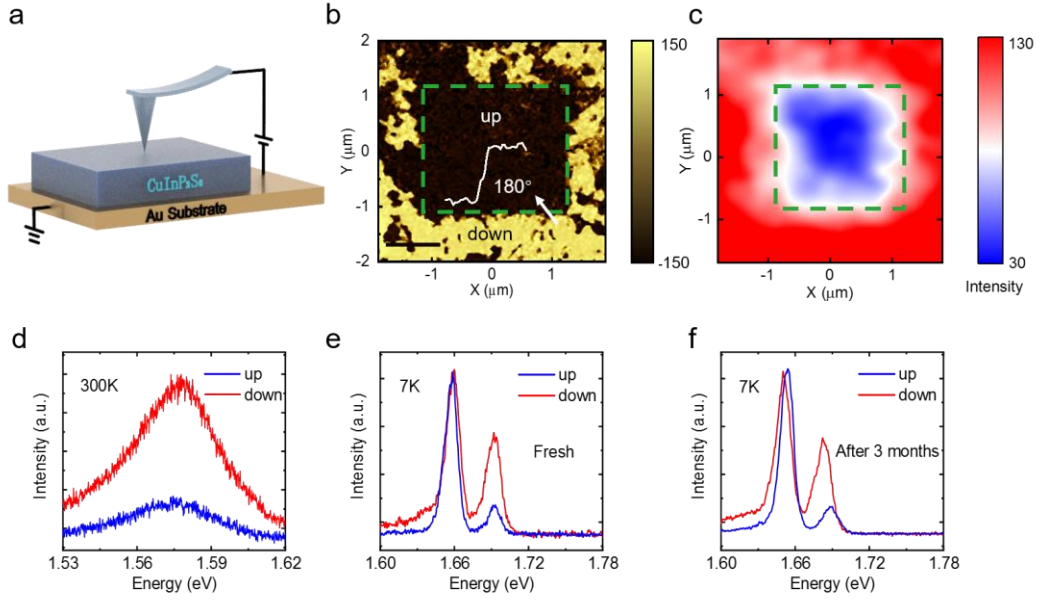


**Figure 3.** Ferroelectric domain imaging by photoluminescence and nonvolatility of ferroelectric CIPS. a) The 3D schematic diagram of the experiment configuration for ferroelectric domain writing. b) The PFM phase image of CIPS with opposite polarization (upward in the box and downward outside the box) written by PFM tip. The scale bar is 1  $\mu\text{m}$ . c) The integral PL intensity mapping of MoSe<sub>2</sub> in the same region at 300 K. The low intensity square corresponds to the upwards polarization region of CIPS. d) PL spectrum of upward (blue line) and downward (red line) area at 300 K and e) 7 K right after PFM writing. f) The PL spectrum of upward (blue line) and downward (red line) area at 7K three months after the PFM writing.

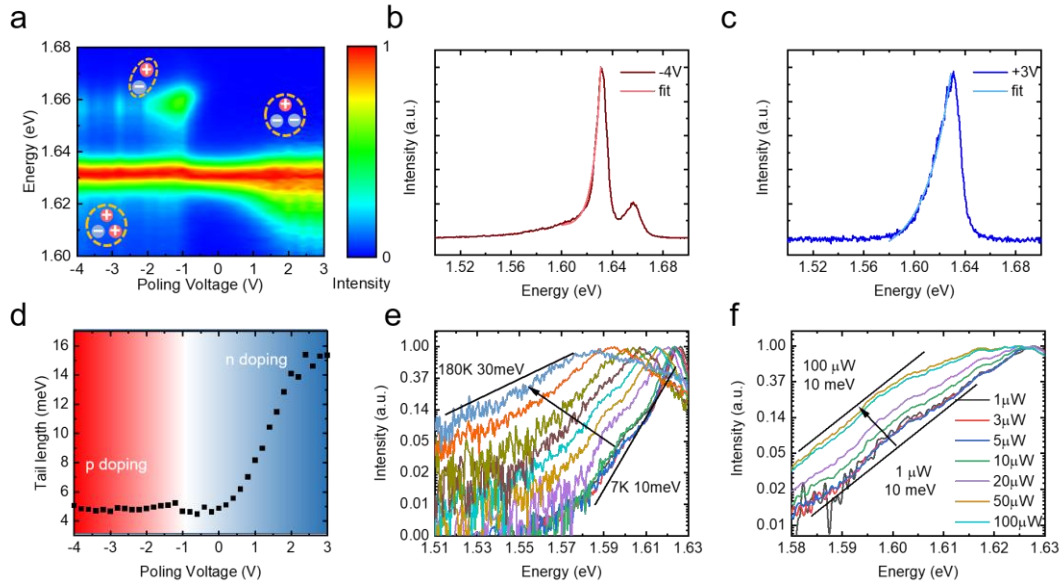


**Figure 4.** Three-body carrier recoil effect in charged excitonic optical transitions. a) The MoSe<sub>2</sub> PL spectrum as the poling voltage changes from -4 V to +3 V. The excitons species are represented by hydrogen and hydrogen ion like models shown in picture. b) The asymmetric PL spectrums of MoSe<sub>2</sub> at +3 V and c) -4 V poling. The pink line in b) and light blue line in c) show the exponential fitting of the low-energy tail of trions peak. d) The fitted tail length of trions peak as a function of the poling voltage. e) Temperature dependence of Trions tail from 7 K to 180 K at +3 V. f) The relationship of Trions tail and laser power at 7 K with +3 V poling voltage.

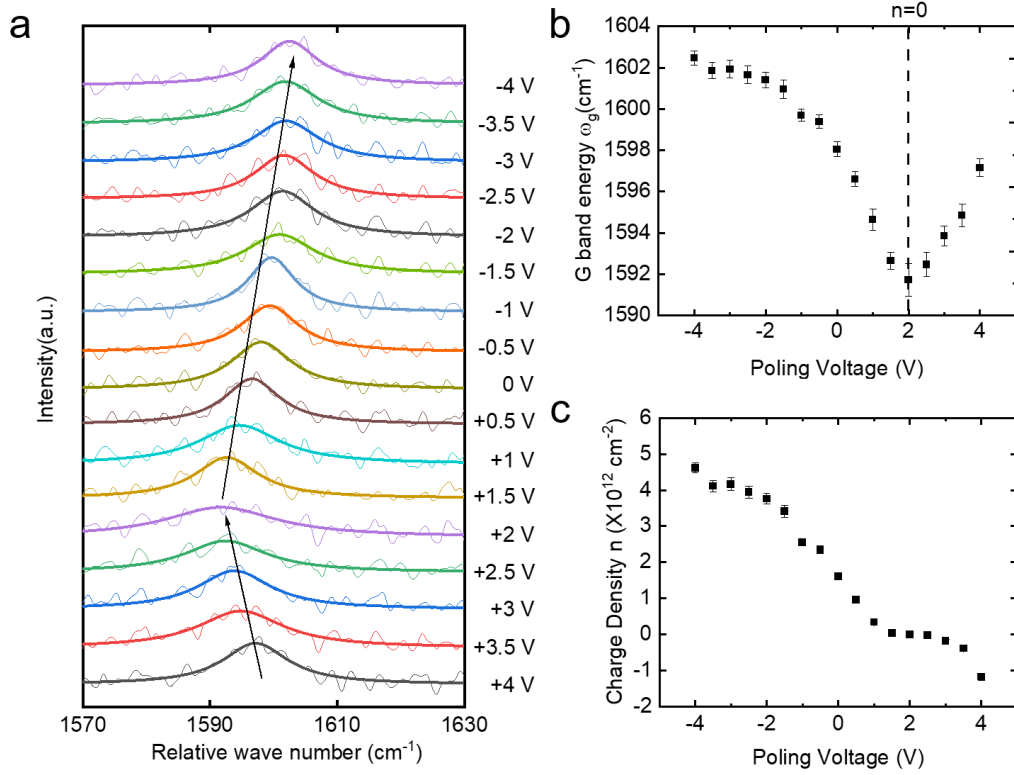


**Figure 5.** Quantification of the charge doping density benchmarked by graphene-CIPS layer hybrid structure. a) The G mode Raman spectrum as poling voltage varies from +4 V to -4 V at 7 K. b) The extracted G mode energy  $\omega_g$  varies with poling voltage. The dashed line indicates the neutral point for graphene. c) The converted charge density in graphene changes with poling voltage.

## References

1. Gong, Y. et al. Band gap engineering and layer-by-layer mapping of selenium-doped molybdenum disulfide. *Nano Lett.* **14**, 442-449 (2014).
2. Ugeda, M. M. et al. Giant bandgap renormalization and excitonic effects in a monolayer transition metal dichalcogenide semiconductor. *Nat. Mater.* **13**, 1091-1095 (2014).
3. Raja, A. et al. Coulomb engineering of the bandgap and excitons in two-dimensional materials. *Nat. Commun.* **8**, 15251 (2017).
4. Zhang, X. X., You, Y., Zhao, S. Y. & Heinz, T. F. Experimental Evidence for Dark Excitons in Monolayer WSe<sub>2</sub>. *Phys. Rev. Lett.* **115**, 257403 (2015).
5. Mak, K. F. et al. Tightly bound trions in monolayer MoS<sub>2</sub>. *Nat. Mater.* **12**, 207-211 (2013).
6. Wang, Z. et al. Evidence of high-temperature exciton condensation in two-dimensional atomic double layers. *Nature* **574**, 76-80 (2019).
7. You, Y., Zhang, X., Berkelbach, T. C., Hybertsen, M. S., Reichman, D. R. & Heinz, T. F. Observation of biexcitons in monolayer WSe<sub>2</sub>. *Nat. Phys.* **11**, 477-481 (2015).
8. Zeng, H., Dai, J., Yao, W., Xiao, D. & Cui, X. Valley polarization in MoS<sub>2</sub> monolayers by optical pumping. *Nat. Nanotechnol.* **7**, 490-493 (2012).
9. Mak, K. F., He, K., Shan, J. & Heinz, T. F. Control of valley polarization in monolayer MoS<sub>2</sub> by optical helicity. *Nat. Nanotechnol.* **7**, 494-498 (2012).
10. Zhu, B., Zeng, H., Dai, J., Gong, Z. & Cui, X. Anomalously robust valley polarization and valley coherence in bilayer WS<sub>2</sub>. *Proc. Natl. Acad. Sci. USA* **111**, 11606-11611 (2014).
11. Mak, K. F., Lee, C., Hone, J., Shan, J. & Heinz, T. F. Atomically thin MoS<sub>2</sub>: a new direct-gap semiconductor. *Phys. Rev. Lett.* **105**, 136805 (2010).
12. Splendiani, A. et al. Emerging photoluminescence in monolayer MoS<sub>2</sub>. *Nano Lett.* **10**, 1271-1275 (2010).
13. Zhang, Y. et al. Direct observation of the transition from indirect to direct bandgap in atomically thin epitaxial MoSe<sub>2</sub>. *Nat. Nanotechnol.* **9**, 111-115 (2014).
14. Chernikov, A. et al. Exciton binding energy and nonhydrogenic Rydberg series in monolayer WS<sub>2</sub>. *Phys. Rev. Lett.* **113**, 076802 (2014).
15. Mouri, S., Miyauchi, Y. & Matsuda, K. Tunable photoluminescence of monolayer MoS<sub>2</sub> via chemical doping. *Nano Lett.* **13**, 5944-5948 (2013).
16. Sercombe, D. et al. Optical investigation of the natural electron doping in thin MoS<sub>2</sub> films deposited on dielectric substrates. *Sci. Rep.* **3**, 3489 (2013).
17. Nan, H. et al. Strong Photoluminescence Enhancement of MoS<sub>2</sub> through Defect Engineering and Oxygen Bonding. *Acs Nano* **8**, 5738-5745 (2014).
18. Ross, J. S. et al. Electrical control of neutral and charged excitons in a monolayer semiconductor. *Nat. Commun.* **4**, 1474 (2013).
19. Ross, J. S. et al. Electrically tunable excitonic light-emitting diodes based on monolayer WSe<sub>2</sub> p-n junctions. *Nat. Nanotechnol.* **9**, 268-272 (2014).
20. Shang, J. et al. Observation of Excitonic Fine Structure in a 2D Transition-Metal Dichalcogenide Semiconductor. *ACS Nano* **9**, 647-655 (2015).
21. Ko, C. Reconfigurable Local Photoluminescence of Atomically-Thin Semiconductors via Ferroelectric-Assisted Effects. *Nanomaterials* **9**, 1620 (2019).
22. Li, C. H., McCreary, K. M. & Jonker, B. T. Spatial Control of Photoluminescence at Room



- Temperature by Ferroelectric Domains in Monolayer  $\text{WS}_2/\text{PZT}$  Hybrid Structures. *ACS Omega* **1**, 1075-1080 (2016).
23. Nguyen, A. et al. Toward Ferroelectric Control of Monolayer  $\text{MoS}_2$ . *Nano Lett.* **15**, 3364-3369 (2015).
  24. Wen, B. et al. Ferroelectric-Driven Exciton and Trion Modulation in Monolayer Molybdenum and Tungsten Diselenides. *ACS Nano* **13**, 5335-5343 (2019).
  25. Bennett, J. W., Grinberg, I. & Rappe, A. M. New Highly Polar Semiconductor Ferroelectrics through d8 Cation-O Vacancy Substitution into  $\text{PbTiO}_3$ : A Theoretical Study. *J. Am. Chem. Soc.* **130**, 17409-17412 (2008).
  26. Lu, H. et al. Enhancement of ferroelectric polarization stability by interface engineering. *Adv. Mater.* **24**, 1209-1216 (2012).
  27. Stengel, M., Vanderbilt, D. & Spaldin, N. A. Enhancement of ferroelectricity at metal-oxide interfaces. *Nat. Mater.* **8**, 392-397 (2009).
  28. Liu, F. et al. Room-temperature ferroelectricity in  $\text{CuInP}_2\text{S}_6$  ultrathin flakes. *Nat. Commun.* **7**, 12357 (2016).
  29. Christopher, J. W., Goldberg, B. B. & Swan, A. K. Long tailed trions in monolayer  $\text{MoS}_2$ : Temperature dependent asymmetry and resulting red-shift of trion photoluminescence spectra. *Sci. Rep.* **7**, 14062 (2017).
  30. Yan, J., Zhang, Y., Kim, P. & Pinczuk, A. Electric field effect tuning of electron-phonon coupling in graphene. *Phys. Rev. Lett.* **98**, 166802 (2007).
  31. Das, A. et al. Monitoring dopants by Raman scattering in an electrochemically top-gated graphene transistor. *Nat. Nanotechnol.* **3**, 210-215 (2008).
  32. Stampfer, C. et al. Raman imaging of doping domains in graphene on  $\text{SiO}_2$ . *Appl. Phys. Lett.* **91**, 241907 (2007).
  33. Ueno, K., Shimotani, H., Yuan, H., Ye, J., Kawasaki, M. & Iwasa, Y. Field-Induced Superconductivity in Electric Double Layer Transistors. *J. Phys. Soc. Jpn.* **83**, 032001 (2014).
  34. Wu, J. et al. High tunnelling electroresistance in a ferroelectric van der Waals heterojunction via giant barrier height modulation. *Nat. Electron.* **3**, 466-472 (2020).
  35. Zhou, Y. et al. Out-of-Plane Piezoelectricity and Ferroelectricity in Layered  $\alpha\text{-In}_2\text{Se}_3$  Nanoflakes. *Nano Lett.* **17**, 5508-5513 (2017).
  36. Castellanos-Gomez, A. et al. Deterministic transfer of two-dimensional materials by all-dry viscoelastic stamping. *2D Mater.* **1**, 011002 (2014).